RESEARCH PAPER

Numerical simulation of laminar non-Newtonian blood flow under varying Reynolds numbers and geometric parameters using OpenFOAM

Mehmet Numan Kaya ⬥ 1,*,‡

1Necmettin Erbakan University, Faculty of Engineering, Department of Mechanical Engineering, 42090 Konya, Türkiye (ROR)

* Corresponding Author
‡ mnkaya@erbakan.edu.tr (Mehmet Numan Kaya)

Abstract

Blood flow within biomedical devices and vascular models is characterized by laminar dynamics at relatively low Reynolds numbers, where shear-dependent viscosity governs hemodynamic behavior. This behavior is commonly observed in biomedical applications, such as nozzles, and accurate modeling is essential. In this study, numerical simulations of laminar non-Newtonian blood flow are performed in OpenFOAM using the Bird–Carreau viscosity model to examine the influence of flow conditions and nozzle geometry. The FDA benchmark nozzle is employed as a reference geometry, and the computational setup is validated against available experimental data prior to the parametric study. Five throat Reynolds numbers, $Re = 100, 300, 500, 1000$, and 1500, are investigated together with two collector cone angles, $20°$ and $40°$, as well as three throat diameters, $D_t = 3, 4$, and 5 mm, to assess geometric effects. The results show that narrower throats and higher Reynolds numbers significantly increase both velocity and shear stress, highlighting the strong sensitivity of hemodynamics to geometric constriction. Pressure drop analysis further reveals that enlarging the throat diameter can substantially reduce losses; for example, at $Re = 1000$ and 1500, increasing the throat from 3 mm to 4 mm lowers the pressure drop by nearly 50%, while a further increase to 5 mm reduces it by about 40%. Overall, the study demonstrates that both geometric variations and flow conditions lead to significant changes in blood flow physics, underscoring their importance in hemodynamic applications.

Keywords: Laminar blood flow; non-newtonian fluid; Bird–Carreau model; CFD; OpenFOAM; blood; Reynolds number; cone angle; throat diameter

AMS 2020 Classification: 76D10; 76D11; 76Z10; 76Z11

1 Introduction

Predicting hemodynamics in biomedical devices and vascular models requires careful consideration of the shear-dependent viscosity of blood, especially under laminar flow conditions at low to

moderate Reynolds numbers [1]. Generalized-Newtonian models such as Carreau/Carreau–Yasuda and Bird–Carreau are widely used because they capture shear-thinning behavior across physiological shear-rate ranges [2]. These models influence key flow features, including pressure losses across constrictions, wall shear stress (WSS) distributions, and the extent of recirculation downstream of expansions and bifurcations. Simplified nozzle geometries are often employed to represent essential characteristics of vascular pathologies, such as throat constrictions and diffusers, and thus provide a controlled setting to study how rheology, flow rate, and geometry interact to influence flow physics [3].

Previous studies have extensively examined the impact of non-Newtonian rheology on vascular and device-related flows, showing its role in pressure distribution, velocity fields, and WSS patterns. Liu et al. [4] compared Newtonian, Casson, and Carreau–Yasuda models in intracranial arterial stenosis and reported rheology-dependent differences in pressure ratios and WSS for both idealized and patient-specific cases. Mamun et al. [5] simulated an idealized 3D stenosis with Carreau and Cross laws, finding that deviations from Newtonian predictions were most pronounced near the throat and during early systole. Mehrabi and Setayeshi [6] applied a power-law model in pulsatile stenoses and showed that increasing severity led to larger pressure jumps and amplified WSS near the neck. Çutay et al. [7] validated stenosis simulations against experiments and demonstrated that even small geometric differences strongly affected pressure drop, recirculation, and WSS, with Carreau predicting higher peak WSS than Newtonian or power-law models. Gijsen et al. [8] investigated a carotid bifurcation under steady flow and reported that non-Newtonian rheology altered WSS patterns compared to Newtonian assumptions. Lakzian and Akbarzadeh [9] studied a curved stenosed artery with a power-law model and found maximal WSS at the neck and higher peaks for shorter lesions, as well as different stability trends for shear-thinning and shear-thickening cases. Fuchs et al. [10] compared Casson, Quemada, and Walburn–Schneck models in the thoracic aorta and observed order-of-magnitude changes in instantaneous viscosity, though the influence on time-averaged WSS was modest except in low-shear regions. Faraji et al. [11] analyzed a patient-specific thoracic aortic aneurysm and found similar overall flow patterns across models but quantitative differences in WSS and OSI, with the power-law model deviating most at high flow. Bilgi and Atalık [12] coupled Carreau rheology with elastic walls in an abdominal aortic aneurysm and showed that Newtonian assumptions overestimated velocities and biased oscillatory indicators, potentially masking degeneration risk. Panchal et al. [13] studied double-fusiform aneurysms and reported that increasing heart rate reduced intra-aneurysmal stasis (RRT) while altering TAWSS and OSI distributions. Johnston et al. [14, 15] provided early evidence of shear-thinning effects in the coronary circulation, while later studies highlighted that oscillatory and transverse WSS are highly sensitive to vessel motion and rheology [16]. In the cerebral circulation, Bernabeu et al. [17] and Oliveira et al. [18] emphasized that non-Newtonian effects become most important in low-shear regions and aneurysm sacs, where Newtonian models can overestimate WSS or misrepresent OSI. More recent comparisons have stressed the need for application-specific rheology choices, showing metric- and severity-dependent performance gaps [19, 20], while network-level simulations demonstrated that including measured inflow and impedance outlets improves physiological accuracy in multibranch anatomies [21]. Classic aneurysm studies further noted that non-Newtonian properties mainly affect shear stresses during peak systole, with only modest influence on pressure under resting conditions [22].

The current study adopts a validated approach by applying the Bird–Carreau model to the FDA benchmark nozzle. Compared with prior studies, the main contributions are to quantify the combined effects of flow and geometry on hemodynamic indicators under shear-thinning conditions, and provide a compact characterization across Reynolds number, cone angle, and throat diameter space to guide model selection and design in biomedical device flows.

2 Material and methods

Numerical approach

Computational fluid dynamics (CFD) was employed to simulate laminar blood flow. The governing equations are the incompressible continuity and momentum equations, given in Eqs. (1) and (2), respectively [23–26].

$$\nabla \cdot \mathbf{U} = 0, \tag{1}$$

$$\rho \left(\frac{\partial \mathbf{U}}{\partial t} + \mathbf{U} \cdot \nabla \mathbf{U} \right) = -\nabla p + \nabla \cdot \left(\mu(\dot{\gamma}) \left[\nabla \mathbf{U} + (\nabla \mathbf{U})^T \right] \right). \tag{2}$$

Here, $\mathbf{U}$ is the velocity vector, p is the pressure, ρ is the density, and $\mu(\dot{\gamma})$ is the shear-rate dependent viscosity.

The viscosity of blood was described using the Eq. (3) [14, 27, 28]:

$$\mu(\dot{\gamma}) = \mu_\infty + (\mu_0 - \mu_\infty) \left[1 + (\lambda \dot{\gamma})^a \right]^{\frac{n-1}{a}}, \tag{3}$$

where μ_0 is the zero-shear viscosity, μ_∞ the infinite-shear viscosity, λ a time constant, a a fitting parameter, and n the power-law index. Density was taken as $\rho = 1056 \, \text{kg/m}^3$.

The shear stress magnitude was computed as given in Eq. (4):

$$|\tau| = \mu(\dot{\gamma}) \, |\dot{\gamma}| = \mu(\dot{\gamma}) \sqrt{\tfrac{1}{2} \, \gamma_{ij} \gamma_{ij}}, \tag{4}$$

where $\gamma_{ij} = \partial_i u_j + \partial_j u_i$ is the shear rate tensor. Mesh generation and simulations were performed using BARAM, a GUI environment built on the open-source OpenFOAM framework [29]. The simulations utilized the buoyantSimpleNFoam solver with the SIMPLE algorithm for pressure-velocity coupling. Boundary conditions were specified as velocity inlet, pressure outlet, and no-slip wall conditions. Convergence was achieved when residuals of flow variables fell below 10^{-5}.

Mesh independence and validation

The FDA benchmark nozzle was selected as the validation model [30, 31]. This geometry consists of a 12 mm inlet diameter, 20° cone angle, 4 mm throat diameter, and a 40 mm throat length, followed by a sudden expansion, representing characteristic features of biomedical flows [32–34]. Figure 1 illustrates the FDA benchmark nozzle geometry with key specifications. The red dashed lines indicate the axial positions of measurement locations used in this study. These locations correspond to the contraction region, throat section, and downstream expansion area, respectively. To ensure grid-converged results, three structured meshes with approximately 10k, 53k, and 82k cells were tested. Axial velocity distributions along the nozzle centerline between $z = -0.1$ m and $z = 0.1$ m were compared and presented in Figure 2. Significant differences were observed between the coarse (10k) mesh and the finer meshes, particularly downstream of the throat ($z > 0$). In contrast, the 53k and 82k cell meshes produced nearly identical velocity profiles. Therefore, the intermediate grid was selected for all subsequent simulations. The selected mesh has a maximum non-orthogonality of about 51 and a maximum skewness of approximately 0.85. A 10-layer
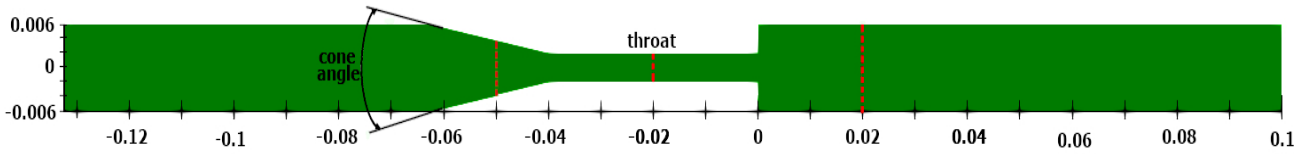
Figure 1. Geometrical Specifications of the FDA Nozzle. The red dashed lines indicate the axial positions of measurement locations used in this study

boundary layer mesh with an expansion ratio of 1.2 was applied near the walls, with a first layer thickness of approximately 0.0005 m.

Following mesh selection, the numerical setup was validated against experimental particle image velocimetry (PIV) measurements at $Re = 500$. Axial velocity distributions along the centerline between $z = -0.1$ m to $z = 0.1$ m were compared between the present CFD results and the reference experimental data of Trias et al. [31] and presented in Figure 3. The comparison showed very good agreement in both magnitude and shape of the velocity profiles, confirming the reliability of the numerical methodology prior to the parametric study.
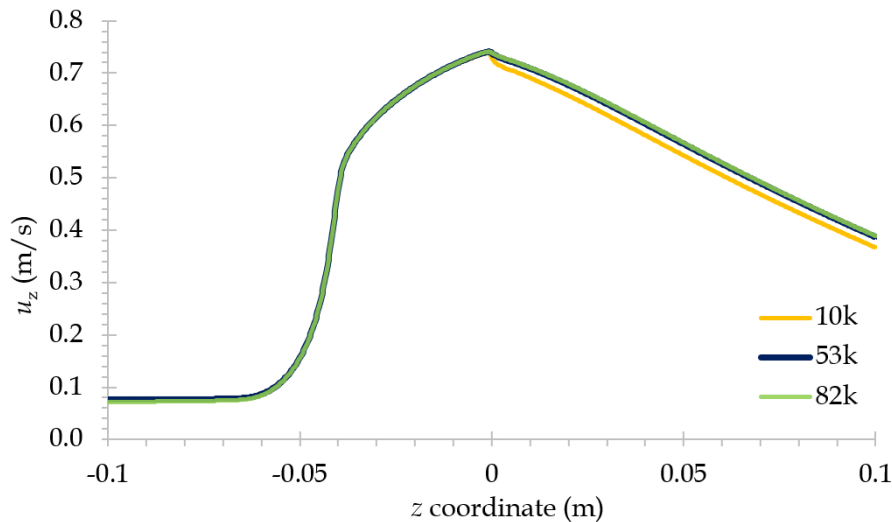

Figure 2. Axial velocity along the nozzle centerline for coarse (10k), medium (53k), and fine (82k) meshes

Investigated parameters

The influence of flow rate was characterized by the throat Reynolds number, defined as given in Eq. (5):

$$Re = \frac{\rho U_t D_t}{\mu},$$ (5)

where U_t is the average velocity at the throat, D_t is the throat diameter, ρ is the density, and μ is the effective viscosity. Five Reynolds numbers were examined: $Re = 100, 300, 500, 1000,$ and 1500. For each case, the inlet velocity was adjusted to achieve the target Reynolds number, ensuring consistency across the parametric study.

In addition to flow rate, nozzle geometry was varied by changing both the cone angle and the throat diameter. Two cone angles, $20°$ and $40°$, were analyzed to evaluate the impact of acceleration in the converging section. Furthermore, three throat diameters, $D_t = 3, 4,$ and 5 mm,
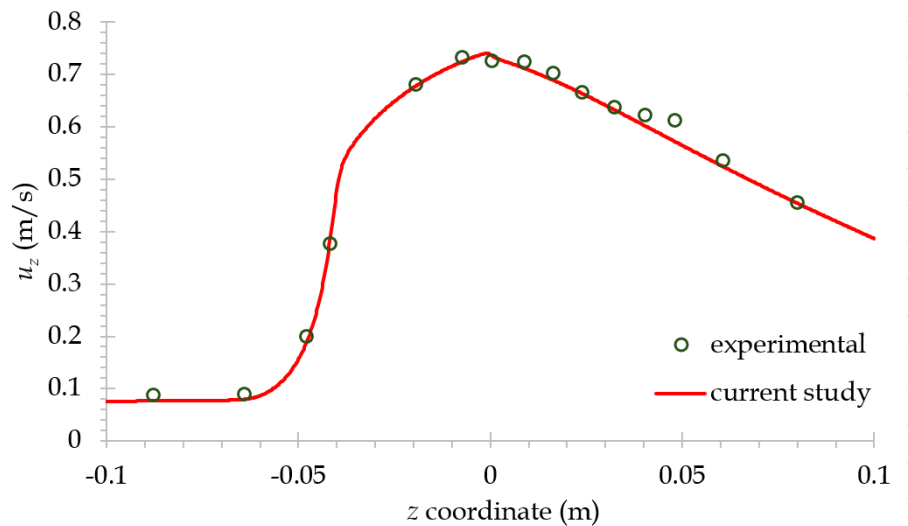
Figure 3. Axial velocity along the nozzle centerline at $Re = 500$: comparison of CFD predictions (current study) with experimental data [31]
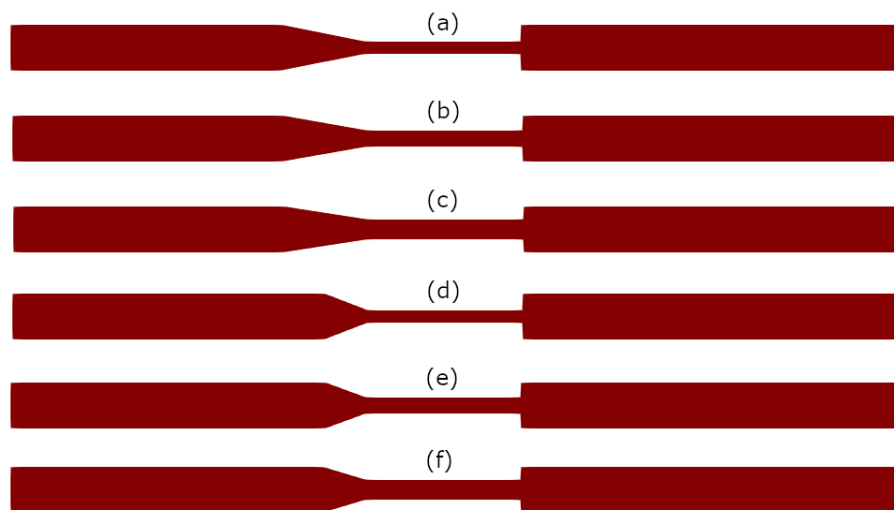
were considered, as illustrated in Figure 4.

Figure 4. Nozzle geometries considered in the parametric study: (a) cone angle 20°, throat $D_t = 3$ mm; (b) cone angle 20°, throat $D_t = 4$ mm; (c) cone angle 20°, throat $D_t = 5$ mm; (d) cone angle 40°, throat $D_t = 3$ mm; (e) cone angle 40°, throat $D_t = 4$ mm; (f) cone angle 40°, throat $D_t = 5$ mm

The selected geometric and flow parameters were chosen to represent physiologically relevant conditions within the laminar regime. The Reynolds number range of 100–1500 corresponds to typical values encountered in small-diameter biomedical devices and vascular models, as also reported in previous benchmark and validation studies of the FDA nozzle. The cone angles of 20° and 40° were selected to capture both gradual and steep acceleration characteristics observed in converging nozzles, allowing a clear comparison of shear and pressure effects. Throat diameters of 3–5 mm were determined to represent a realistic range of throat sizes while preserving laminar behavior across all cases.

3 Results and discussion

In this section, the results are presented to highlight the key hemodynamic mechanisms within the nozzle geometry. Figure 5 illustrates the axial pressure drop along the centerline, normalized by the inlet pressure. Subplots (a), (c), and (e) correspond to the $20°$ cone angle, while (b), (d), and (f) represent the $40°$ case. Throat diameters of 3, 4, and 5 mm are shown in pairs (a,b), (c,d), and (e,f), respectively. The results indicate that higher Reynolds numbers produce substantially larger pressure losses, particularly downstream of the throat. In addition, smaller throat diameters lead to sharper drops in pressure due to the stronger acceleration required to conserve mass. Quantitatively, at $Re = 1000$ and 1500, the pressure drop decreases by nearly 50% when the throat diameter increases from 3 mm to 4 mm, and by a further 40% when increased from 4 mm to 5 mm. The influence of cone angle is also clear: a $40°$ contraction generates a more rapid pressure change compared to the smoother $20°$ transition.
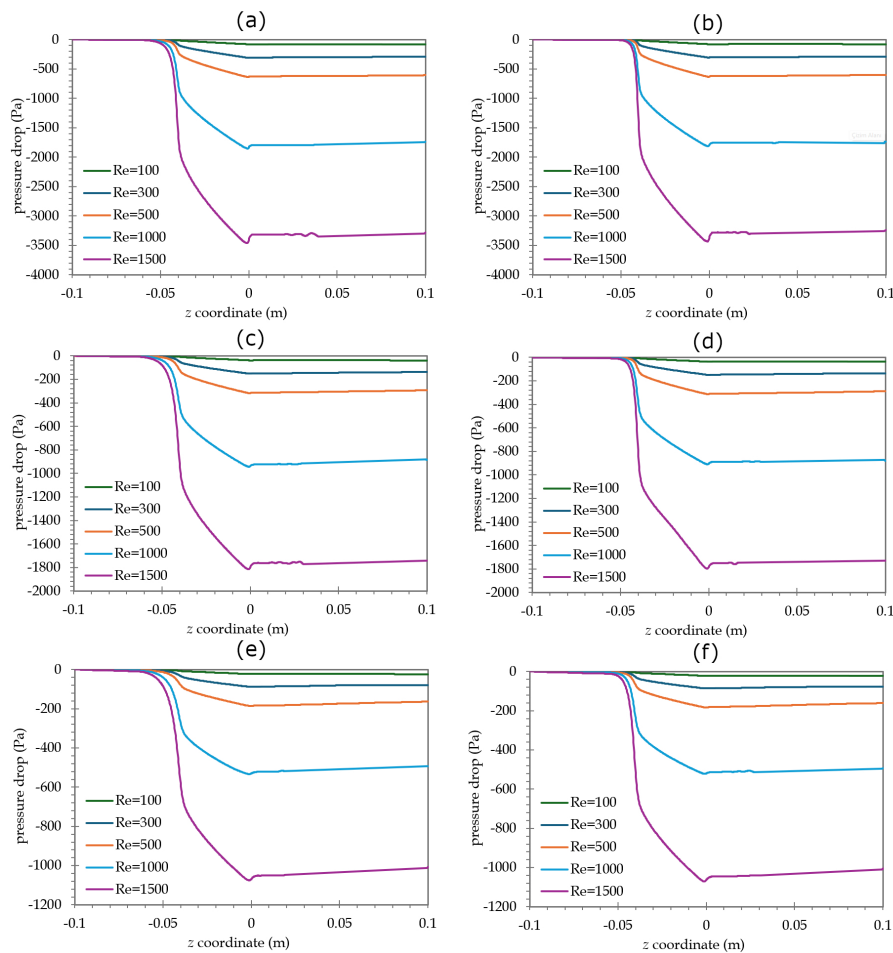

Figure 5. Pressure drop along the nozzle centerline relative to inlet pressure. Subplots (a,c,e) correspond to $20°$ cone angle, and (b,d,f) to $40°$ cone angle. Pairs (a,b), (c,d), and (e,f) represent throat diameters of 3, 4, and 5 mm, respectively

Figure 6 shows the velocity distribution along the nozzle centerline. Subplots are organized similarly, with (a,c,e) for the $20°$ cone angle and (b,d,f) for the $40°$ cone angle, across throat diameters of 3, 4, and 5 mm. As expected, higher Reynolds numbers yield higher peak axial velocities. Narrow throats generate longer jet cores, while wider throats produce more diffused profiles. As expected, increasing the throat diameter reduces the velocity magnitude, whereas

increasing Reynolds number raises the peak velocity. For both cone angles, the overall velocity trends are similar, but noticeable differences appear near the contraction region around $z = -0.05$, where the 40° case exhibits a sharper acceleration compared to the smoother 20° transition. The sharper 40° contraction therefore amplifies centerline velocity peaks compared to the 20° configuration, consistent with the stronger pressure gradients observed in Figure 5.
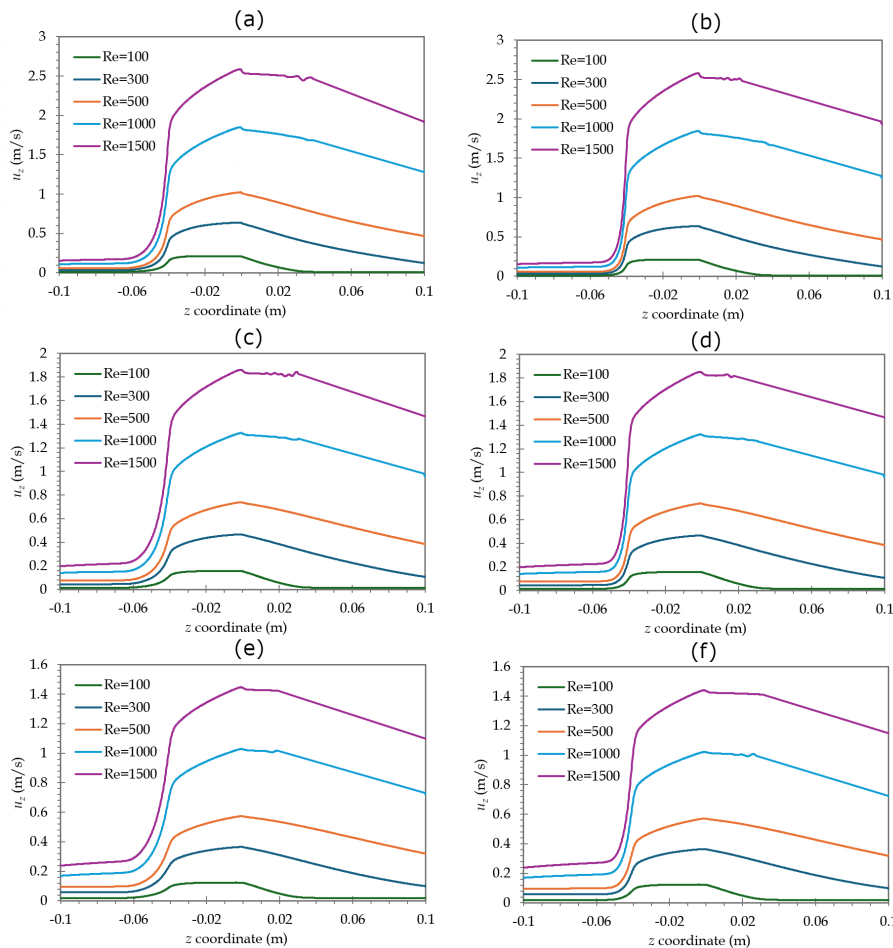

Figure 6. Velocity distribution along the nozzle centerline. Subplots (a,c,e) correspond to 20° cone angle, and (b,d,f) to 40° cone angle. Pairs (a,b), (c,d), and (e,f) represent throat diameters of 3, 4, and 5 mm, respectively

Figure 7 presents velocity contours for throat diameters of 3, 4, and 5 mm (left to right). The upper rows correspond to the 20° cone angle and the lower rows to the 40° case. The color maps reveal the formation of high-speed jets emerging from the throat region. As can be seen from the figure, higher Reynolds numbers and smaller throat diameters produce noticeably stronger velocity peaks immediately downstream of the contraction. For the 20° cone angle, the acceleration occurs more gradually, whereas the 40° configuration generates a sharper jet with a more rapid velocity increase.

Figure 8 depicts radial velocity profiles at three axial locations: $z = -0.05$ m (a,d,g), $z = -0.02$ m (b,e,h), and $z = 0.02$ m (c,f,i), for the 20° cone angle. Rows correspond to throat diameters of 3, 4, and 5 mm, respectively. The position $z = -0.05$ represents the contraction region, $z = -0.02$ corresponds to the throat, and $z = 0.02$ lies just downstream of the sudden expansion. At $z = 0.02$, following the expansion, flow reversal is observed beyond approximately $r = 0.0025$ m for $D_t = 3$ mm, $r = 0.0030$ m for $D_t = 4$ mm, and $r = 0.0035$ m for $D_t = 5$ mm. Within the throat, both increasing Reynolds number and reducing throat diameter leads to higher peak
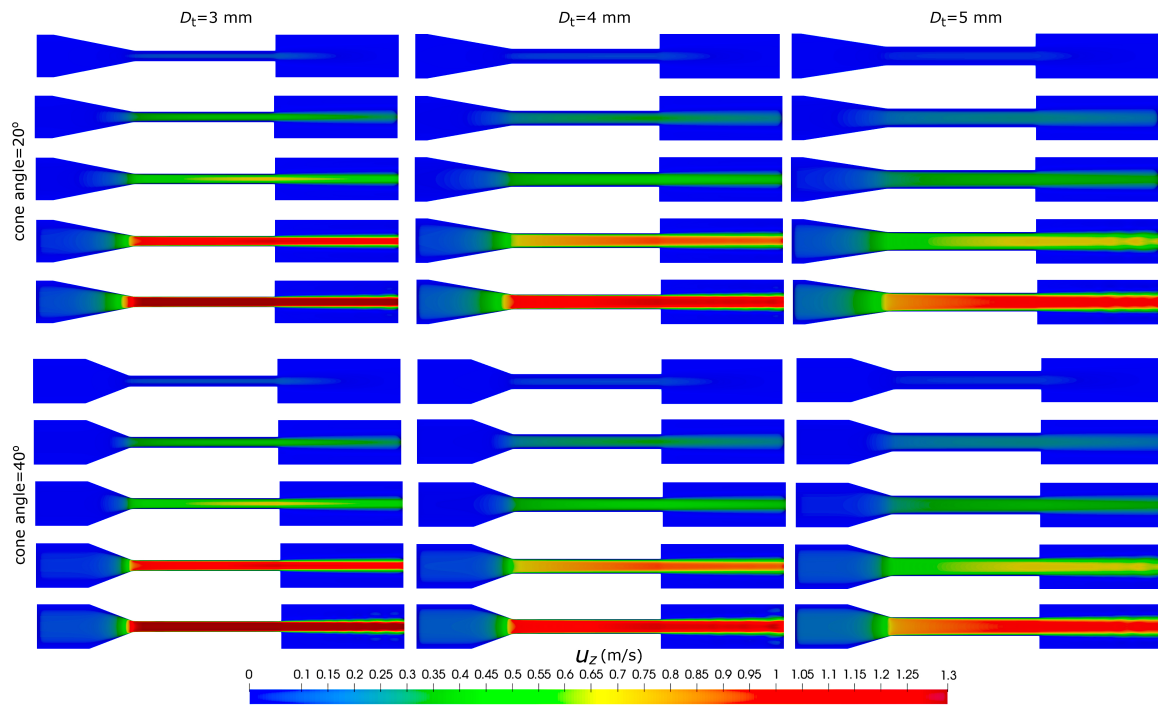
Figure 7. Velocity contours for throat diameters $D_t = 3, 4, 5$ mm (left to right). The upper row corresponds to the 20° cone angle and the lower row to the 40° cone angle
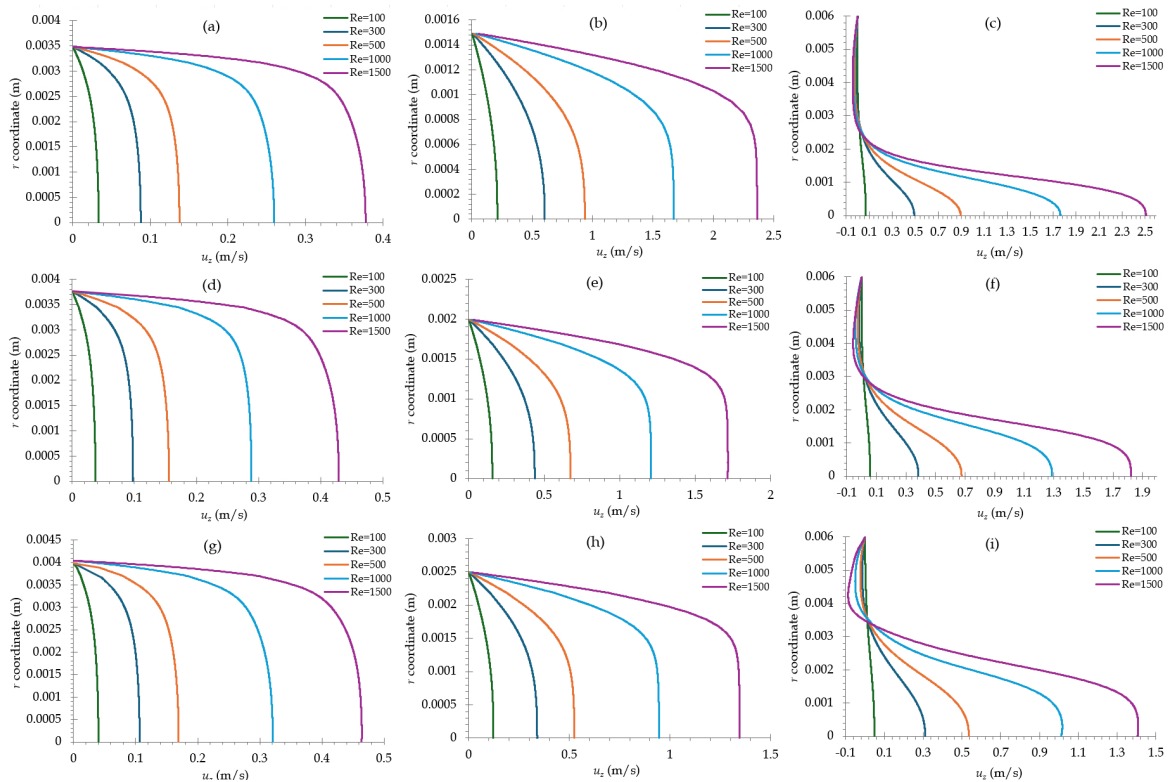

Figure 8. Radial velocity profiles at $z = -0.05$ m (a,d,g), $z = -0.02$ m (b,e,h), and $z = 0.02$ m (c,f,i) for the 20° cone angle. Rows correspond to throat diameters of 3 mm (a,b,c), 4 mm (d,e,f), and 5 mm (g,h,i)

velocities, emphasizing the combined influence of flow rate and geometric constriction on velocity distribution.

Figure 9 presents radial velocity distributions at the same axial locations as those in Figure 8,

but for the 40° cone angle. The profiles exhibit less steep gradients in the contraction region ($z = -0.05$) compared to the 20° case. Similar to the observations for the previous figure, at the throat position, both increasing Reynolds number and reducing throat diameter consistently yield higher peak velocities. Downstream of the sudden expansion, reverse flow zones are observed at larger radial positions, indicating that a larger throat diameter delays the onset of recirculation. Specifically, recirculation begins beyond approximately $r = 0.0025$ m for $D_t = 3$ mm, $r = 0.0030$ m for $D_t = 4$ mm, and $r = 0.0035$ m for $D_t = 5$ mm, with the effect becoming more pronounced as the Reynolds number increases.
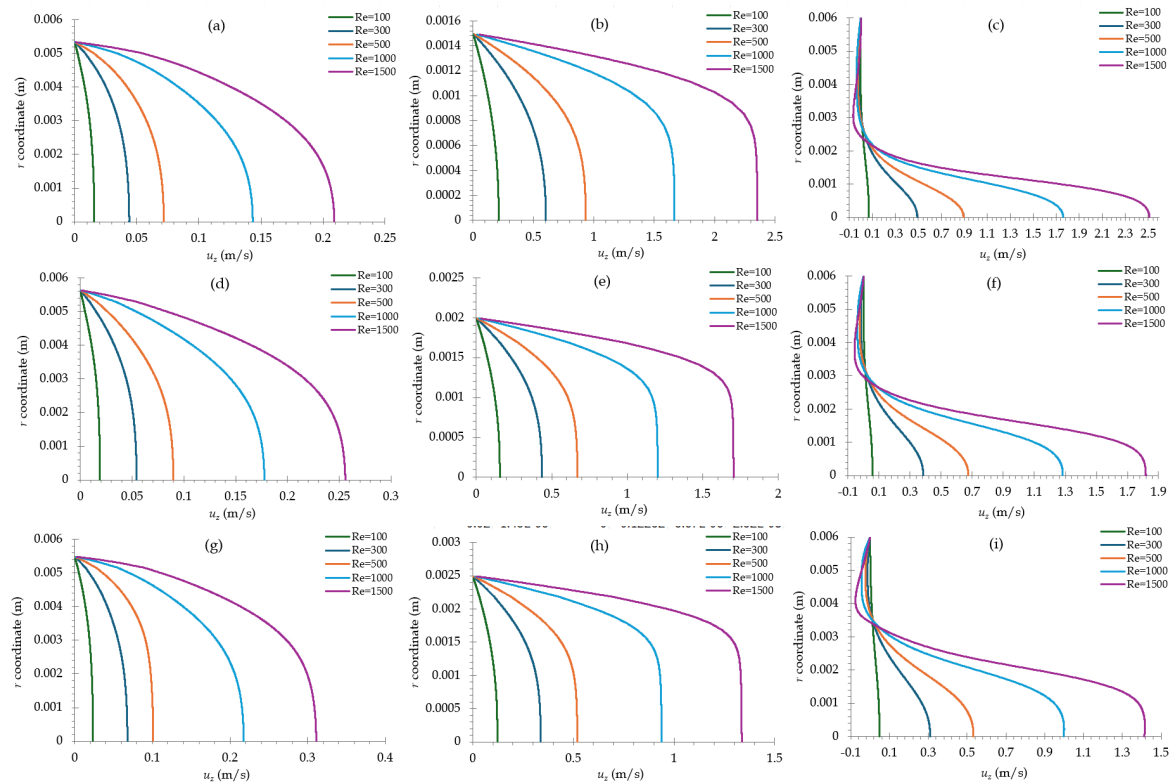

Figure 9. Radial velocity profiles at $z = -0.05$ m (a,d,g), $z = -0.02$ m (b,e,h), and $z = 0.02$ m (c,f,i) for the 40° cone angle. Rows correspond to throat diameters of 3 mm (a,b,c), 4 mm (d,e,f), and 5 mm (g,h,i)

Figure 10 presents the shear stress distributions at the axial locations $z = -0.05, -0.02$, and 0.02 m for the 20° cone angle. Rows correspond to throat diameters of 3, 4, and 5 mm, respectively. Shear stress magnitudes increase with Reynolds number and peak at the wall for $z = -0.05$ and -0.02 m. At $z = 0.02$ m, peak values are obtained around $r = 0.0015$ m, where the peak radial coordinate shifts towards higher r values with increasing throat diameter. Additionally, at $z = 0.02$ m, the curves are wider for larger throat diameters, meaning that the radial distance between minimum and maximum values is larger, and the curves approach zero at higher r values for larger throat diameters. Wider throats reduce the maximum stresses; for instance, when the throat diameter increases by 1 mm, the peak shear stress at $Re = 1500$ decreases by approximately 30%. The influence of Reynolds number is also evident: increasing Re from 500 to 1000 amplifies shear stress by nearly a factor of three, emphasizing the strong coupling between flow rate and near-wall stresses in the contraction region.

Finally, Figure 11 shows the shear stress distributions for the 40° cone angle. Similar to the 20° case, the shear stress magnitudes increase with Reynolds number and exhibit similar peak locations at the wall for $z = -0.05$ and -0.02 m. At $z = 0.02$ m, peak values are again obtained
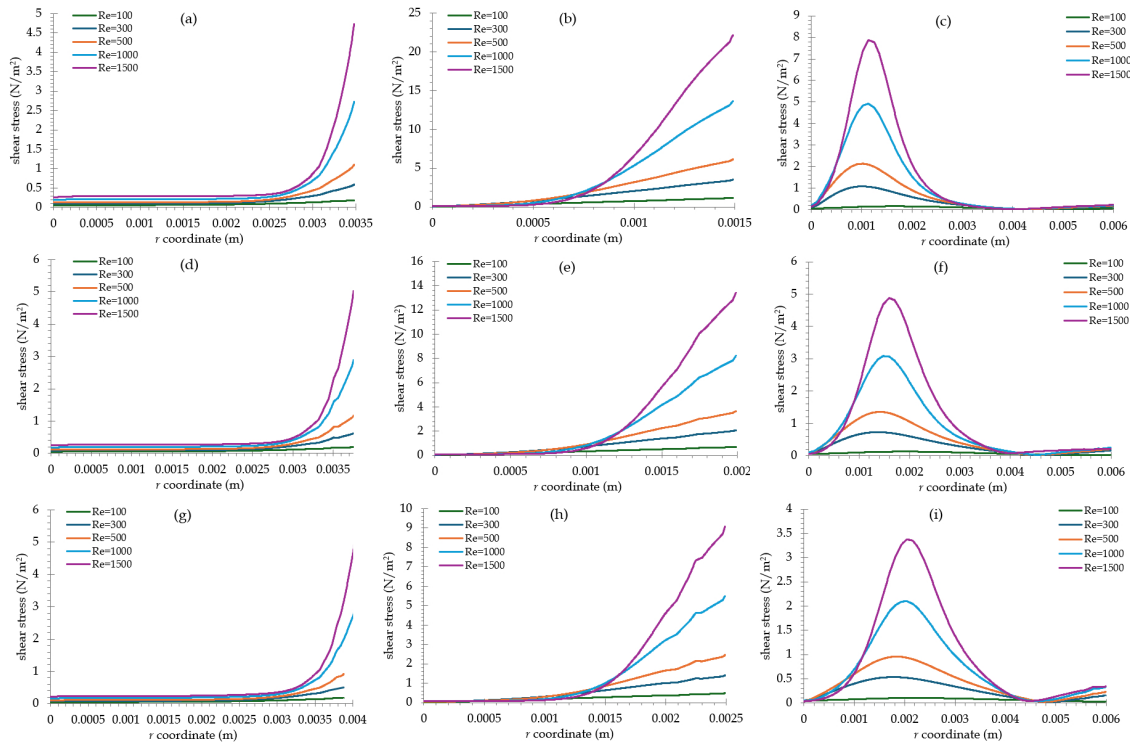
Figure 10. Shear stress distributions at $z = -0.05$ m (a,d,g), $z = -0.02$ m (b,e,h), and $z = 0.02$ m (c,f,i) for the 20° cone angle. Rows correspond to throat diameters of 3 mm (a,b,c), 4 mm (d,e,f), and 5 mm (g,h,i)

Figure 11. Shear stress distributions at $z = -0.05$ m (a,d,g), $z = -0.02$ m (b,e,h), and $z = 0.02$ m (c,f,i) for the 40° cone angle. Rows correspond to throat diameters of 3 mm (a,b,c), 4 mm (d,e,f), and 5 mm (g,h,i)
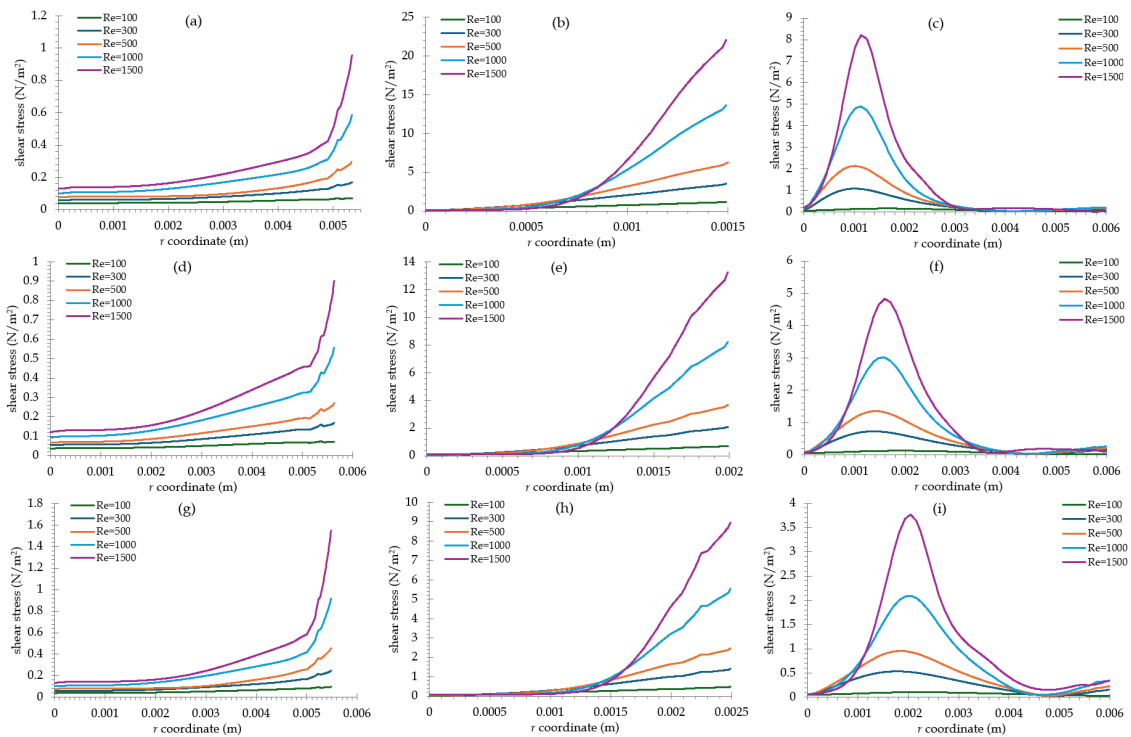
around $r = 0.0015$ m, with the peak radial coordinate shifting towards higher r values as the throat diameter increases. At the contraction region ($z = -0.05$ m), shear stress increases more

gradually for the 40° cone compared to the 20° case. This difference becomes more pronounced at higher Reynolds numbers, where velocity gradients intensify. Overall, smaller diameters and higher Reynolds numbers naturally increase shear stresses, and the cone angle plays a role in controlling the rate of acceleration. The findings confirm that both geometric and flow parameters must be considered in biomedical device design.

4 Conclusion

The present study investigated laminar non-Newtonian blood flow through nozzle geometries derived from the FDA benchmark, focusing on the combined effects of Reynolds number, throat diameter, and cone angle. The simulations demonstrated that pressure losses increased substantially with Reynolds number, rising from about -400 Pa at $Re = 300$ to nearly -2000 Pa at $Re = 1500$ for a 4 mm throat. At higher Reynolds numbers, throat diameter had a strong influence: enlarging the throat from 3 mm to 4 mm at $Re = 1500$ reduced the pressure drop by nearly 50%, while a further increase to 5 mm lowered it by an additional 40%. Steeper cone angles produced sharper acceleration over shorter distances, resulting in stronger velocity gradients compared with smoother contractions. Velocity analysis revealed that peak centerline velocities reached approximately 2.5 m/s at $Re = 1500$ for the 3 mm throat, compared to only 0.3 m/s at $Re = 100$. Wider throats reduced the jet intensity and shortened the high-velocity core, while the 40° cone angle configuration promoted faster flow acceleration than the 20° case. Shear stress distributions highlighted the combined effect of geometry and Reynolds number. At $Re = 1500$, peak shear stress exceeded 20 N/m^2 for the 3 mm throat but remained under 10 N/m^2 for the 5 mm throat, while at $Re = 100$, the maximum shear stress was below 5 N/m^2 for the 3 mm throat case. Increasing Re from 500 to 1000 nearly tripled shear stress values, whereas each 1 mm increase in throat diameter reduced peak stresses by about 30%. The 40° cone angle further intensified shear development earlier in the contraction, with the effect becoming especially pronounced at high Reynolds numbers. In summary, the results confirm that both flow rate and nozzle geometry play an important role in hemodynamic behavior. Pressure losses, velocity distributions, and shear stresses all depend sensitively on throat size, cone angle, and Reynolds number. The findings emphasize the need to balance flow conditions and geometry to manage shear, acceleration, and pressure characteristics, as these factors strongly influence blood flow physics.

Declarations

Use of AI tools

The author declares that he has not used Artificial Intelligence (AI) tools in the creation of this article.

Data availability statement

All data generated or analyzed during this study are included in this article.

Ethical approval

The author states that this research adheres to the ethical standards. This research does not involve either human participants or animals.

Consent for publication

Not applicable

References

[1] Onder, A., Incebay, O. and Yapici, R. Computational fluid dynamics simulating of the FDA benchmark blood pump with different coefficient sets and scaler shear stress models used in the power-law hemolysis model. *Journal of Artificial Organs*, 28, 184-191, (2025). [CrossRef]

[2] Mustafaoğlu, M., Kotçioğlu, İ. and Yeşilyurt, M.K. Numerical analysis of the three-dimensional model of pulsatile and non-Newtonian blood flow in a carotid artery with local occlusion. *Mathematical Modelling and Numerical Simulation With Applications*, 5(1), 97-116, (2025). [CrossRef]

[3] Avci, M. CFD-Based extensional stress and hemolysis risk evaluation in the U.S. food and drug administration (FDA) benchmark nozzle configurations. *Fluids*, 10(9), 224, (2025). [CrossRef]

[4] Liu, H., Lan, L., Abrigo, J., Ip, H.L., Soo, Y., Zheng, D. et al. Comparison of Newtonian and non-Newtonian fluid models in blood flow simulation in patients with intracranial arterial stenosis. *Frontiers in Physiology*, 12, 718540, (2021). [CrossRef]

[5] Mamun, K., Rahman, M.M., Akhter, M.N. and Ali, M. Physiological non-Newtonian blood flow through single stenosed artery. *AIP Conference Proceedings* 1754(1), 040001, (2016). [CrossRef]

[6] Mehrabi, M. and Setayeshi, S. Computational fluid dynamics analysis of pulsatile blood flow behavior in modelled stenosed vessels with different severities. *Mathematical Problems in Engineering*, 2012(1), 804765, (2012). [CrossRef]

[7] Çutay, A., Çermik, Ö. and Kaya, A. Evaluation of the vessel with different stenosis structures using CFD approach. *Kahramanmaraş Sütçü İmam Üniversitesi Mühendislik Bilimleri Dergisi*, 28(1), 245-257, (2025). [CrossRef]

[8] Gijsen, F.J.H., van de Vosse, F.N. and Janssen, J.D. The influence of the non-Newtonian properties of blood on the flow in large arteries: steady flow in a carotid bifurcation model. *Journal of Biomechanics*, 32(6), 601-608, (1999). [CrossRef]

[9] Lakzian, E. and Akbarzadeh, P. Numerical investigation of unsteady pulsatile Newtonian/non-Newtonian blood flow through curved stenosed arteries. *Bio-Medical Materials and Engineering*, 30(5–6), 525-540, (2020). [CrossRef]

[10] Fuchs, A., Berg, N., Fuchs, L. and Prahl Wittberg, L. Assessment of rheological models applied to blood flow in human thoracic aorta. *Bioengineering*, 10(11), 1240, (2023). [CrossRef]

[11] Faraji, A., Sahebi, M. and SalavatiDezfouli, S. Numerical investigation of different viscosity

models on pulsatile blood flow of thoracic aortic aneurysm (TAA) in a patient-specific model. *Computer Methods in Biomechanics and Biomedical Engineering*, 26(8), 986-998, (2022). [CrossRef]

[12] Bilgi, C. and Atalık, K. Numerical investigation of the effects of blood rheology and wall elasticity in abdominal aortic aneurysm under pulsatile flow conditions. *Biorheology*, 56(1), 51-71, (2019). [CrossRef]

[13] Panchal, P.M., Hathi, D.S., Shah, N.K. and Lakdawala, A.M. A numerical study on pulsatile non-Newtonian hemodynamics in double-fusiform abdominal aortic aneurysms. *Physics of Fluids*, 34(3), 031908, (2022). [CrossRef]

[14] Johnston, B.M., Johnston, P.R., Corney, S. and Kilpatrick, D. Non-Newtonian blood flow in human right coronary arteries: steady state simulations. *Journal of Biomechanics*, 37(5), 709-720, (2004). [CrossRef]

[15] Johnston, B.M., Johnston, P.R., Corney, S. and Kilpatrick, D. Non-Newtonian blood flow in human right coronary arteries: transient simulations. *Journal of Biomechanics*, 39(6), 1116-1128, (2006). [CrossRef]

[16] Kandangwa, P., Torii, R., Gatehouse, P.D., Sherwin, S.J. and Weinberg, P.D. Influence of right coronary artery motion, flow pulsatility and non-Newtonian rheology on wall shear stress metrics. *Frontiers in Bioengineering and Biotechnology*, 10, 962687, (2022). [CrossRef]

[17] Bernabeu, M.O., Nash, R.W., Groen, D., Carver, H.B., Hetherington, J., Krüger, T. and Coveney, P.V. Impact of blood rheology on wall shear stress in a model of the middle cerebral artery. *Interface Focus*, 3(2), 20120094, (2012). [CrossRef]

[18] Oliveira, I., Santos, G.B., Gasche, J.L., Militzer, J. and Baccin, C.E. Non-Newtonian blood modeling in intracranial aneurysm hemodynamics: impact on the WSS and OSI metrics for ruptured and unruptured cases. *Journal of Biomechanical Engineering*, (2021).

[19] Singh, D. and Singh, S. Computational analysis of patient-specific pulsatile blood flow: The influence of non-Newtonian models on wall shear stress assessment. *Physics of Fluids*, 36(1), 013123, (2024). [CrossRef]

[20] Liu, S., Wang, S., Tian, H., Xue, J., Guo, Y., Yang, J. et al. Comparison of blood viscosity models in different degrees of carotid artery stenosis. *PeerJ*, 13, e19336, (2025). [CrossRef]

[21] Peng, C., Liu, J., He, W., Qin, W., Yuan, T., Kan, Y. et al. Numerical simulation in the abdominal aorta and the visceral arteries with or without stenosis based on 2D PCMRI. *International Journal for Numerical Methods in Biomedical Engineering*, 38(3), e3569, (2021). [CrossRef]

[22] Khanafer, K.M., Gadhoke, P., Berguer, R. and Bull, J.L. Modeling pulsatile flow in aortic aneurysms: effect of non-Newtonian properties of blood. *Biorheology*, 43(5), 661-679, (2006). [CrossRef]

[23] Manolesos, M., Celik, Y., Ramsay, H., Karande, R., Wood, B., Dinwoodie, I. et al. Performance improvement of a Vestas V52 850kW wind turbine by retrofitting passive flow control devices. *Journal of Physics: Conference Series*, 2767(2), 022027, (2024). [CrossRef]

[24] Kaya, M.N., Satcunanathan, S., Meinke, M. and Schröder, W. Leading-edge noise mitigation on a rod–airfoil configuration using regular and irregular leading-edge serrations. *Applied Sciences*, 15(14), 7822, (2025). [CrossRef]

[25] Kaya, M.N. Numerical Investigation of Hydrofoil Cavitation Using OpenFOAM: Effect of Thickness and Camber. *Black Sea Journal of Engineering and Science*, 8(5), 1585-1594, (2025). [CrossRef]

[26] Kocaaslan, O., Güleren, K.M., Saracoğlu, B.H. and Yasa, T. Dönen patlama motorlarındaki

oluşan dalga yapısının sayısal olarak incelenmesi. *Journal of Thermal Science and Technology*, 44(1), 33-45, (2024). [CrossRef]

[27] Carreau, P.J. Rheological equations from molecular network theories. *Transactions of the Society of Rheology*, 16(1), 99-127, (1972). [CrossRef]

[28] Cho, Y.I. and Kensey, K.R. Effects of the non-Newtonian viscosity of blood on flows in a diseased arterial vessel. Part 1: Steady flows. *Biorheology*, 28(3-4), 241-262, (1991). [CrossRef]

[29] GitHub Repository, NextFOAM: BARAM. [https://github.com/nextfoam/baram], [Accessed: 14/09/2024]

[30] Hariharan, P., Giarra, M., Reddy, V., Day, S.W., Manning, K.B., Deutsch, S. et al. Multilaboratory particle image velocimetry analysis of the FDA benchmark nozzle model to support validation of computational fluid dynamics simulations. *Journal of Biomechanical Engineering*, 133(4), 041002, (2011). [CrossRef]

[31] Trias, M., Arbona, A., Massó, J., Miñano, B. and Bona, C. FDA's nozzle numerical simulation challenge: non-Newtonian fluid effects and blood damage. *PLoS One*, 9(3), e92638, (2014). [CrossRef]

[32] Krishnamoorthy, G. and Gholizadeh, N. Blood damage analysis within the FDA benchmark nozzle geometry at laminar conditions: Prediction sensitivities to software and non-Newtonian viscosity models. *Symmetry*, 16(9), 1165, (2024). [CrossRef]

[33] Fang, P., Wu, P., Feng, H. and Huang, H. Enhancing thrombosis prevention in medical devices: The role of turbulence in washout performance using FDA benchmark nozzle model. *Computer Methods and Programs in Biomedicine*, 261, 108647, (2025). [CrossRef]

[34] Malinauskas, R.A., Hariharan, P., Day, S.W., Herbertson, L.H., Buesen, M., Steinseifer, U. et al. FDA benchmark medical device flow models for CFD validation. In *American Society for Artificial Internal Organs (ASAIO) Platinum 70th Anniversary Special Edition* (pp. 317-327). Boca Raton, USA: CRC Press, (2024).

How to cite this article: Kaya, M.N. (2025). Numerical simulation of laminar non-Newtonian blood flow under varying Reynolds numbers and geometric parameters using OpenFOAM. *Bulletin of Biomathematics,* 3(2), 150-163. https://doi.org/10.59292/bulletinbiomath.1791463